

## Article

# Phased Array Ultrasonic Sector Scan Imaging of Helicopter Damper Bolts Based on Vector Coherence Factor

Jingxing Huang <sup>1</sup>, Ming Chen <sup>2</sup>, Qingru Kong <sup>2</sup>, Liangzhong Xiao <sup>1</sup>, Chao Lu <sup>2</sup> and Yao Chen <sup>2,\*</sup><sup>1</sup> Changhe Aircraft Industries Group Co., Ltd., Jingdezhen 333002, China<sup>2</sup> Key Laboratory of Non-Destructive Testing Technology, Ministry of Education, Nanchang Hangkong University, Nanchang 330063, China

\* Correspondence: chenyaon@nchu.edu.cn; Tel.: +86-187-7988-0057

**Abstract:** Non-destructive testing of the cracks on the in-service bolt's shank with size M18 is a challenging technical problem. Due to the weak echo energy of cracks with large buried depths, the conventional phased array ultrasonic sector scan imaging has a low signal-to-noise ratio, resulting in the effective defect echo submerged in the structural wave of bolts. This work proposes a method of phased array ultrasonic sector scan imaging based on vector coherence factors to detect the microcracks on the surface of the bolt shank. This is achieved by weighting the phased array sector scan imaging with the vector coherence factor to detect the microcracks of the in-service helicopter damper bolt. Experimental work is also carried out to contrast the SNR value of cracks at buried depths of 70 mm and 90 mm with traditional phased array ultrasonic sector scanning images. This demonstrates that the proposed phased array ultrasonic sector scan imaging based on vector coherence factors detected the cracks with a depth of 0.1 mm at the buried depth of 90 mm. The SNR value of the cracks at the buried depth 70 mm in DAS\_VCF images is improved by 11.67 dB, compared with the traditional DAS images, in the case of the focus depth at 60 mm.



**Citation:** Huang, J.; Chen, M.; Kong, Q.; Xiao, L.; Lu, C.; Chen, Y. Phased Array Ultrasonic Sector Scan Imaging of Helicopter Damper Bolts Based on Vector Coherence Factor. *Appl. Sci.* **2022**, *12*, 9936. <https://doi.org/10.3390/app12199936>

Academic Editor: Giuseppe Lacidogna

Received: 4 August 2022

Accepted: 27 September 2022

Published: 2 October 2022

**Publisher's Note:** MDPI stays neutral with regard to jurisdictional claims in published maps and institutional affiliations.



**Copyright:** © 2022 by the authors. Licensee MDPI, Basel, Switzerland. This article is an open access article distributed under the terms and conditions of the Creative Commons Attribution (CC BY) license (<https://creativecommons.org/licenses/by/4.0/>).

**Keywords:** bolt shank; crack; ultrasonic; sector scanning; vector coherence factor

## 1. Introduction

The helicopter hub damper bolt is an essential fastener on the helicopter propeller system and plays a role in connecting, positioning, and so on. During the helicopter service, serious safety accidents may occur from bolt fatigue resulting from the damper bolt shanks being subjected to alternating loads for a long time [1]. Hence, the safe operation of the helicopter needs to undergo regular non-destructive testing and evaluate the service life of fatigue crack initiation and the propagation life of the damper bolt shank [2,3].

Currently, the common non-destructive testing method is to remove the bolt and then detect the bolt with magnetic particle testing or penetrant testing [4–6]. However, these methods have the disadvantages of a heavy workload, long detection cycle, and low efficiency [7]. More importantly, potential safety risks for helicopters may exist due to improper commissioning during bolt disassembly and reassembly. Therefore, in the presence of in-service bolts, non-destructive testing of fatigue cracks on the bolt shanks of in-service dampers is of great significance for ensuring the safe operation of helicopters and reducing the working intensity of operators.

With strong penetration ability, fast detection speed, and strong detection mobility, ultrasonic testing is a non-destructive method widely used in metal material flaw detection [8]. However, the ultrasonic beam is difficult to shoot into the crack root of the bolt effectively due to its narrow and tall structure. When using the conventional ultrasonic testing method to detect the cracks of bolt shanks, missed detection and misjudgment of cracks are easily caused by the pseudo defects and interference wave from waveform conversion [9].

Compared with the conventional ultrasonic method, phased array ultrasonic testing technology has advantages, including optional deflection angle of the sound beam, adjustable focusing depth, and high detection sensitivity [10,11]. At present, fatigue cracks of bolt shanks have been detected with ultrasonic testing in the port [12], nuclear power [13], and other industries. For example, defect echoes of cracks can be intuitively distinguished from the structural interference wave in the ultrasonic detection of in-service bolt shanks, combined with the signal characteristics of phased array S-scan imaging and A-scan in the ultrasonic view [14]. Compared with conventional ultrasonic testing, implementation of the phased array ultrasonic S-scan detection method improves the detection accuracy and reduces the rate of missed detection and misjudgment caused by the detection personnel.

Generally, the diameter of port bolts is larger than M30 [12]. It has been shown that ultrasonic detection of cracks in port bolt shanks requires the detection accuracy to reach a 0.5 mm depth [15]. By contrast, compared with the bolts used in ports, nuclear power, and other fields, the service conditions of helicopter damper bolts are more stringent. Hence, to ensure the safe operation of the helicopter hub, it is necessary to detect more minor cracks in damper bolts effectively [16]. Moreover, there is a high demand for the detection of deeper cracks due to the bolt shank size of the helicopter damper M18 × 120. However, due to the weak echo energy of cracks with large buried depths, the conventional ultrasonic phased array S-scan imaging has the problem of a low signal-to-noise ratio, resulting in the effective defect echo submerged in the structural wave of the bolts [17].

In terms of improving the signal-to-noise ratio, researchers have carried out lots of efforts [18–20]. Among them, adaptive coherent weighting [21] is a common post-processing imaging method which calculates the weighting coefficient according to the coherence of the echo signal of each pixel and carries out coherent weighting on the original DAS (delayed and sum) signal. Compared with the signal-to-noise of the original image, adaptive coherent weighting improves the signal-to-noise ratio of TFM [22] (total focusing method) and CPWC [23] (coherent plane wave compounding) images. At present, adaptive coherent weighted imaging technology has been widely used in CPWC and TFM imaging. In contrast with CPWC and TFM, the adaptive coherent weighting of phased array ultrasonic sector scan imaging requires the calculation of the phase information of RF signals at each phase angle.

In addition, noise resulting from the structure of the bolt shank and pseudo defects will disturb the identification of real defects. Therefore, the adaptive weighting methods based on amplitude of signal is not applicable to the detection of such components [24]. In contrast with the adaptive weighting method based on ratio and standard deviation [25,26], a series of adaptive weighting method based on instantaneous phase is proposed and widely used in plane wave imaging [27] and the total focusing method [28,29]. Among them, VCF (vector coherence factor), a phase coherent weighting factor, is proposed by Camacho et al. [23] and is more sensitive to the phase of the signal and suitable for the coherent weighting of sector scan RF signal data at each phase angle compared with the adaptive weighting factor based on amplitude of the signal. However, there is no literature report about phase-coherent weighted imaging of phased array sector scans.

In this paper, we firstly apply VCF to phased array sector scan imaging to detect microcracks with large buried depths effectively and improve the signal-to-noise ratio of the crack images. In addition, the phased array ultrasonic detection ability of the helicopter bolt shank crack is analyzed and demonstrated by the echo response of the artificial groove. Furthermore, the crack detection limit of the key loaded position of the damper bolt screw crack is determined and then provides theoretical and practical guidance for the bolt safety service evaluation.

## 2. Principle

### 2.1. Phased Array Ultrasonic Sector Scan Imaging

A schematic diagram of the beam forming process for phased array sector scanning imaging is shown in Figure 1. Assume that the linear array consists of  $N$  elements, whose

index number is  $n(1 \leq n \leq N)$ , and the center distance between the adjacent two elements is  $d_{pitch}$ . Figure 1a shows that the coordinate system  $xOz$  is established with the array center as the coordinate origin. The array element arrangement direction and screw depth direction are the positive directions of the  $x$ -axis and  $z$ -axis, respectively. Let there be a total of  $M$  emission angles and keep the focal length  $D_F$  constant. The  $k$ th emission angle focuses on point  $F$  at the sound speed  $c_l$ , and the deflection angle between point  $F$  and the  $z$ -axis is  $|\theta_k|$ . Then, the delay time  $\tau_n$  of the  $n$ th array element is given by:

$$\tau_n = \frac{D_F}{c_l} \left[ 1 - \sqrt{1 + \left( \frac{nd_{pitch}}{D_F} \right)^2 - 2 \frac{nd_{pitch}}{D_F} \sin|\theta_k|} \right] \tag{1}$$

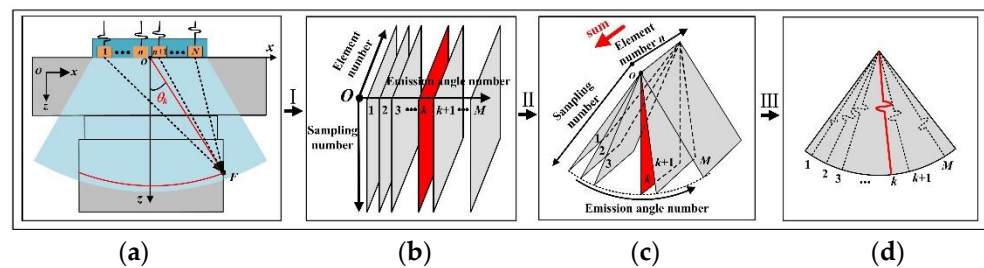


**Figure 1.** Schematic diagram of phased array sector scan beam-forming process. (a) Beam steering and focusing, (b) signal acquisition, (c) coordinate transformation, and (d) sector scanning imaging display.

In the unit of emission angle, the RF signal is stored in the form of a 2-D data matrix  $N_f \times N$ , where  $N_f$  represents the number of samples, as shown in Figure 1b. After coordinate transformation, the ultrasonic sector scanning imaging shown in Figure 1d can be obtained by adding along the direction of the array elements. Then, the amplitude of the RF signal at the  $k$ th emission angle  $\theta_k$  can be expressed as:

$$I_{\theta_k} = \sum_{n=1}^N S_{\tau n} \tag{2}$$

where  $S_{\tau n}$  is the delayed data received by the  $n$ th array element at the  $k$ th emission angle  $\theta_k$ .

### 2.2. Vector Coherence Factor

According to the Euler formula, the complex signal can be given by the formula  $S = |h|(\cos\varphi + i \sin\varphi)$ , where  $|h|$  represents the mode length of the signal and  $i$  denotes  $i^2 = -1$ . When  $|h|$  is equal to 1, the complex signal only contains phase information. On the angular scale, the complex signal can be regarded as the unit vector  $X_n = (\cos\varphi_n, \sin\varphi_n)$ , which can be represented by phase angle  $\varphi_n$ . For the unit vector sample  $\{X_1, X_2, \dots, X_N\}$  of size  $N$ , the length of its mean resultant vector can be expressed as:

$$|R| = \sqrt{a^2 + b^2} \in [0, 1] \tag{3}$$

where  $a$  and  $b$  respectively represent the real part and imaginary part of the resultant vector, which are expressed as:

$$a = \frac{1}{N} \sum_{n=1}^N \cos \varphi_n, \quad b = \frac{1}{N} \sum_{n=1}^N \sin \varphi_n \tag{4}$$

According to Equation (3), the length  $|R|$  of the mean resultant vector can represent the distribution consistency of the phase angle  $\varphi$ . As shown in Figure 2, when  $|R|$  approaches 1, it indicates that all angles are concentrated in a specific direction. When

the value of  $|R|$  is very small or even close to 0, it shows that the unit vector samples are randomly distributed, and the direction consistency of the phase angle is poor.

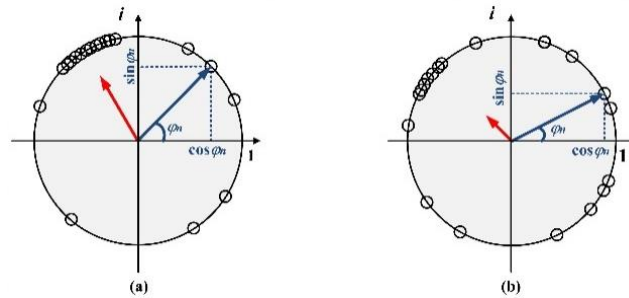


**Figure 2.** Schematic diagram of phase angle distribution consistency represented by vector coherence factor. (a) Centralized distribution and (b) random distribution.

2.3. Sector Scan Imaging Based on Vector Coherence Factor

The processing object of sector scan imaging coherent weighting is an A–scan signal at each emission angle. For the sector scan emission angle  $\theta_k$ , the flow chart of the coherent weighting of the A–scan signal is shown in Figure 3.

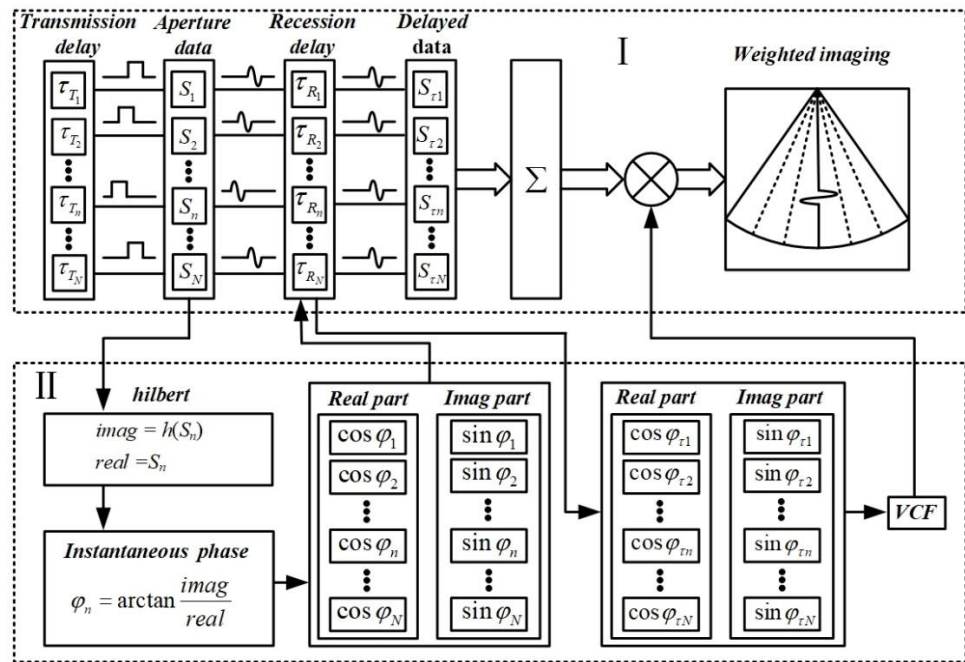


**Figure 3.** Flow chart of VCF weighted S–scan post-processing imaging principle.

At the  $k$ th emission angle, aperture data  $\{S_1, \dots, S_N\}$  represents the RF signals received by the  $n$ th array element. According to circular statistics, the instantaneous phase angle of  $\{S_1, \dots, S_N\}$  can be regarded as the angles sample  $\{j_1, \dots, j_N\}$ . Then the unit circle is composed of cosine and sine values of the instantaneous phase. Under this condition, as shown in Figure 3, the process of the VCF weighting for sector scan images is as follows:

Step I: By recession delay processing for the aperture data  $\{S_1, \dots, S_N\}$ , the signal amplitude slice set  $\{S_{\tau 1}, \dots, S_{\tau N}\}$  of delayed data is summed and forms an A–Scan signal for imaging in  $k$ th emission angle;

Step II: Before recession delay, extract the  $\{\cos j_{\varphi_{\tau 1}}, \dots, \cos j_{\varphi_{\tau N}}\}$  and  $\{\sin j_{\varphi_{\tau 1}}, \dots, \sin j_{\varphi_{\tau N}}\}$  components from  $\{S_1, \dots, S_N\}$  by Equation (5). Then, the VCF weighting factor for sector scan imaging is obtained using Equation (6). According to Equation (7), the summed A–Scan signals for imaging with  $k$ th emission are weighted by VCF and finally form the weighted sector scan image.

The instantaneous phase  $\varphi_n$  can be expressed as:

$$\varphi_n = \arctan \frac{\text{imag}}{\text{real}} = \arctan \frac{h(S_n)}{S_n} \quad (5)$$

According to Equations (3) and (4), another expression of  $|R|$  of the mean resultant vector length in sector scan imaging, i.e., the VCF of the A–Scan signal for  $\theta_k$ , is as follows:

$$VCF_{\theta_k} = \sqrt{\left(\frac{1}{N} \sum_{n=1}^N \cos \varphi_{\tau n}\right)^2 + \left(\frac{1}{N} \sum_{n=1}^N \sin \varphi_{\tau n}\right)^2} \quad (6)$$

Then, the A–scan signal with emission angle  $\theta_k$  is weighted by VCF, and the expression of the sector scan image is:

$$I_{\theta_k-VCF} = I_{\theta_k} \cdot VCF_{\theta_k} \quad (7)$$

According to Equations (3)~(6), it is not difficult to find that VCF is a method to reflect the degree of phase coherence through the mean resultant vector length, and its value range is  $[0, 1]$ . At a certain emission angle, when the phase of the delayed signals of all array elements is highly consistent, the VCF tends to 1; on the contrary, when the phase of the delayed signal is randomly distributed, the VCF tends to 0.

Furthermore, VCF can be used as a weighting factor for beam–forming image reconstruction, and the factor itself can be directly used for imaging. At the same time, the adaptive beam–forming process can also be performed by multiplying the conventional image and the coherent image.

### 3. Experiment

#### 3.1. Instrument Introduction

As shown in Figure 4, The phased array ultrasonic S–scan imaging equipment is a Vantage 32LE system from Verasonics in the US, and the probe is connected with the 32–channel interface of the signal acquisition system. The acoustic beam emission angle is  $-30^\circ \sim 30^\circ$ , with an interval of  $1^\circ$ , a total of 61 emission angles. The sampling frequency is 62.5 MHz, and the propagation speed of the sound wave in the bolt is 5900 m/s. Five focusing depths, 30 mm, 40 mm, 50 mm, 60 mm, and 70 mm, were set to explore the influence of focusing depth on imaging results. The model of the linear array ultrasonic transducer is 15L32–0.25  $\times$  10 from Guangdong Shantou Ultrasonic Electronics Co., Ltd., in Shantou City, Guangdong Province. as shown in Figure 5. The main parameters of the transducer are shown in Table 1.

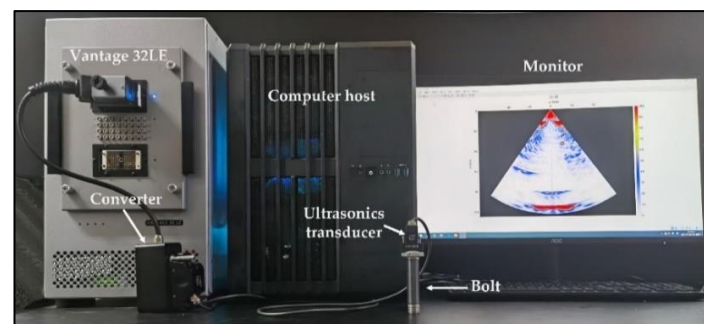


**Figure 4.** The phased array ultrasonic S–scan signal acquisition system.

The probe is in direct contact with the end face of the nut. The oil is used as the coupling agent between the probe and the nut to realize the contact detection, ignoring the influence of the coupling agent on the detection results. Make the echo at the bottom of the thread symmetrical about the central axis of the sector image, and take the echo at the bottom of the thread and the sidewall of the bolt in the figure as the reference. Then,

according to the high amplitude echo on the sidewall of the screw, rotate the probe's position to determine the crack's position on the sidewall of the bolt. In the vicinity of the bolt sidewall crack, the probe was slowly rotated to adjust the amplitude of the defect to weaken the deformation wave caused by the reflection and refraction of the bolt sidewall. Finally, the probe was fixed, and the raw data were collected for ultrasonic phased array sector scanning imaging.

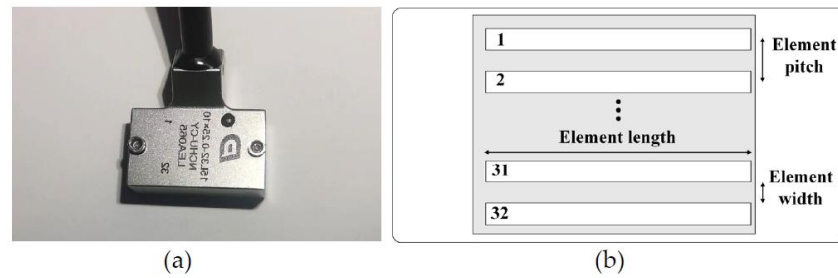


Figure 5. Linear array ultrasonic transducer. (a) Ultrasonic transducer and (b) array distribution diagram.

Table 1. Parameters of Phased Array.

Parameter	Value
Element pitch (mm)	0.25
Element width (mm)	0.2
Element length (mm)	10
Center frequency (MHz)	15
Number of elements	32

3.2. Materials

The raw material of the experiment is the helicopter hub damper bolt, as shown in Figure 6. The surface of the bolt shank has a tungsten carbide coating with a thickness of 0.2 mm. The main parameters of the bolt are shown in Table 2. To simulate real cracks, the artificial grooves were machined on the surface of the bolt shank in this work. The parameters of the artificial grooves are shown in Table 3.

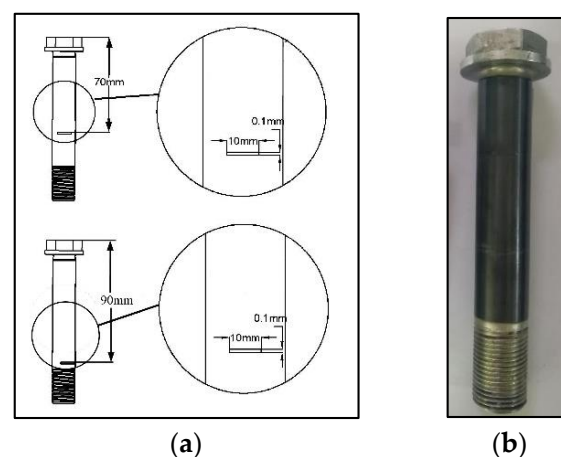


Figure 6. Helicopter hub damper bolts and artificial grooves. (a) Main parameters of grooves and (b) bolt.

**Table 2.** Main parameters of bolts.

Parameter	Value
Nut diameter (mm)	30
Nut height (mm)	14
Bolt shank diameter (mm)	18
Bolt shank length (mm)	90
Bolt length (mm)	120

**Table 3.** Main parameters of two artificial grooves.

Parameters	Buried Depth <sup>1</sup>	Groove Depth	Groove Width	Groove Length
Value (mm)	70.00	0.10	0.10	10.00
	90.00	0.10	0.10	10.00

<sup>1</sup> Buried depth refers to the height difference between the artificial groove and the upper-end face of the nut.

### 3.3. Image Quality Index

According to Equations (5)~(7), the traditional sector image of the bolt sidewall cracks is processed by VCF weighting and imaged using MATLAB. SNR was used to evaluate the magnitude difference between the defect signal in the image and its surrounding noise signal. The definition of SNR is as follows:

$$SNR = 20 \log_{10} \left( \frac{I_s}{I_n} \right) \tag{8}$$

where  $I_s$  and  $I_n$  represent the average intensity of the signal and background noise in a specific imaging area, respectively.

## 4. Results and Analysis

### 4.1. Imaging Results

A set of experiments was carried out to verify the validity of vector coherence factor weighting. Images are shown on a logarithmic scale with a dynamic range of 100 dB. Figures 7 and 8 show the images of grooves with a depth of 0.1 mm, and the buried depths of 70 mm and 90 mm, respectively.

Figure 7 (left) shows original images obtained with phased array ultrasonic S-scan imaging without further processing, including (a), (d), (g), (j), and (m), whose focus depths are 30 mm, 40 mm, 50 mm, 60 mm, and 70 mm, respectively. As shown in the red rectangle in Figure 7a, the sidewall secondary echo caused by waveform conversion is seen in the middle of the sector-scan image, while the reflected echo of the sidewall on the bolt shank is vaguely observed. The defect echo of crack appears on the sidewall of the bolt shank, located at the depth of 70 mm and can be intuitively distinguished from the structural interference wave in the DAS images.

Figure 7 (middle) shows the images of VCF weighting factors, including (b), (e), (h), (k), and (n) with focus depths of 30 mm, 40 mm, 50 mm, 60 mm, and 70 mm, respectively. All of the defect echoes, reflected echoes of the sidewall on the bolt shank, and artifacts caused by waveform conversion are seen in the middle of the VCF image.

Figure 7 (right) shows S-scan images weighted by the VCF, including (c), (f), (i), (l), and (o) with focus depths of 30 mm, 40 mm, 50 mm, 60 mm, and 70 mm, respectively. Dynamic range and signal-to-noise rate improve with regard to original S-scan images. Moreover, both amplitudes of background noise and artifacts caused by waveform conversion are reduced in the DAS\_VCF image. Moreover, in both cases with VCF weights or without, the display of defects in the DAS\_VCF image is clearer with the focus depth increasing. However, due to the attenuation of acoustic energy, the echo of defects at 90 mm depth is less than 70 mm.

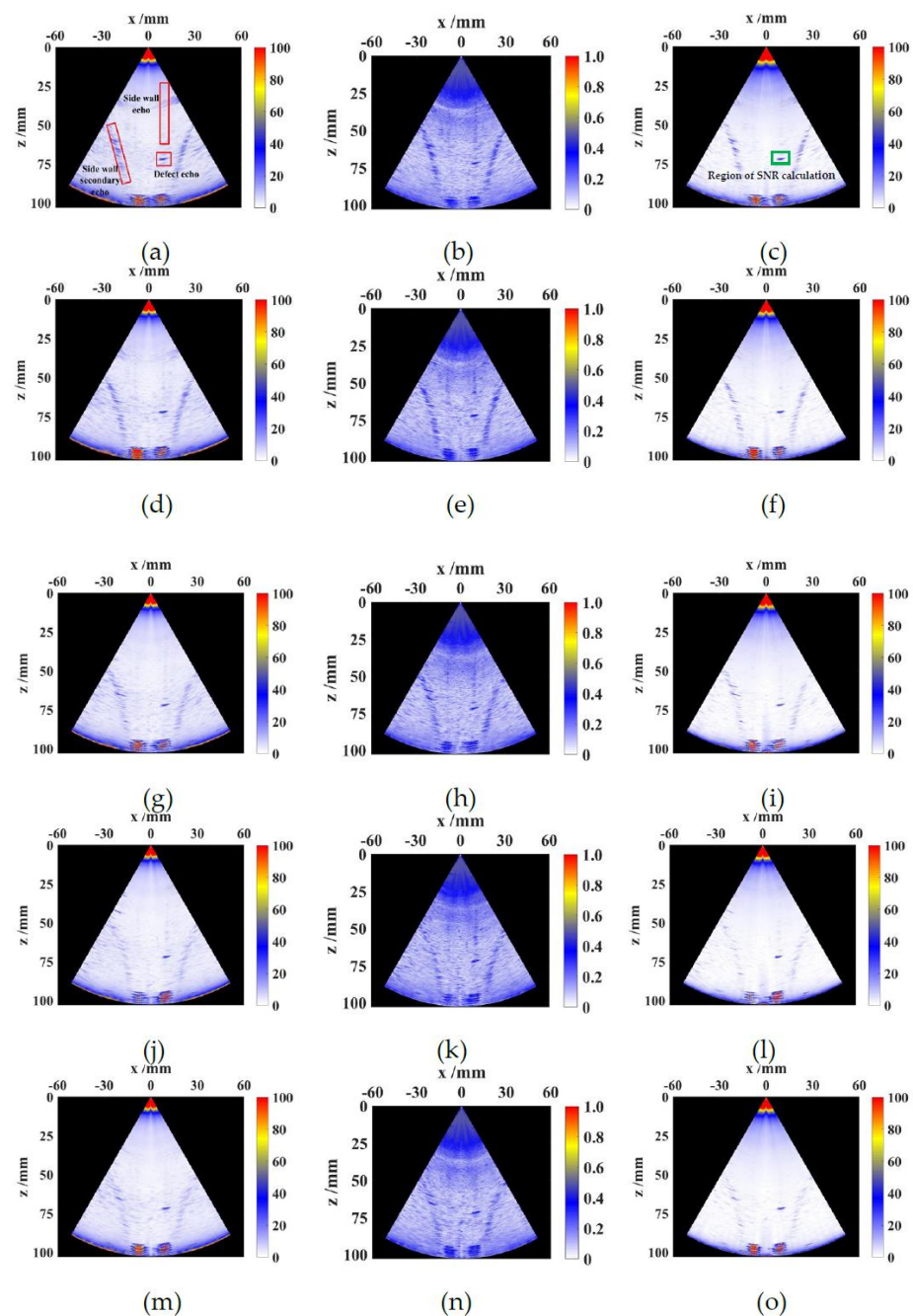


**Figure 7.** Imaging results of groove with depth 0.1 mm and buried depth 70 mm. (a) DAS, (b) VCF, and (c) DAS\_VCF with focus depth 30 mm; (d) DAS, (e) VCF, and (f) DAS\_VCF with focus depth 40 mm; (g) DAS, (h) VCF, and (i) DAS\_VCF with focus depth 50 mm; (j) DAS, (k) VCF, and (l) DAS\_VCF with focus depth 60 mm; (m) DAS, (n) VCF, and (o) DAS\_VCF with focus depth 70 mm.

Mostly, the size of the crystal grain for the heterogeneous medium is smaller than the wavelength. In contrast, the continuous interface of steel-air is equivalent to a large scatter. Therefore, the received signals of the pulse–echo are mainly from the sidewall of the bolt shank, and little from the bolt inside, thus the VCF in the sidewall echo higher than inside. While in the case that there is a groove on the surface of the bolt shank, the consistency of phase for defect is highest, i.e., the value of VCF factor of the groove is highest and close to 1 and that of the medium scattering signal is close to 0, as shown in Figure 7b.

Furthermore, in addition to the noise introduced by the inhomogeneous medium, there is very strong electrical noise in the image, as shown in the orange rectangle of Figure 8m. In the process of detection, a large transmission voltage and time–gain compensation are required due to the large defect with a deeply buried depth, and a strong noise is introduced by a large transmission voltage and time–gain compensation. However, as shown in Figure 7c, the noise in the image can be eliminated basically after VCF weighting due to the value of the VCF factor of noise being low.

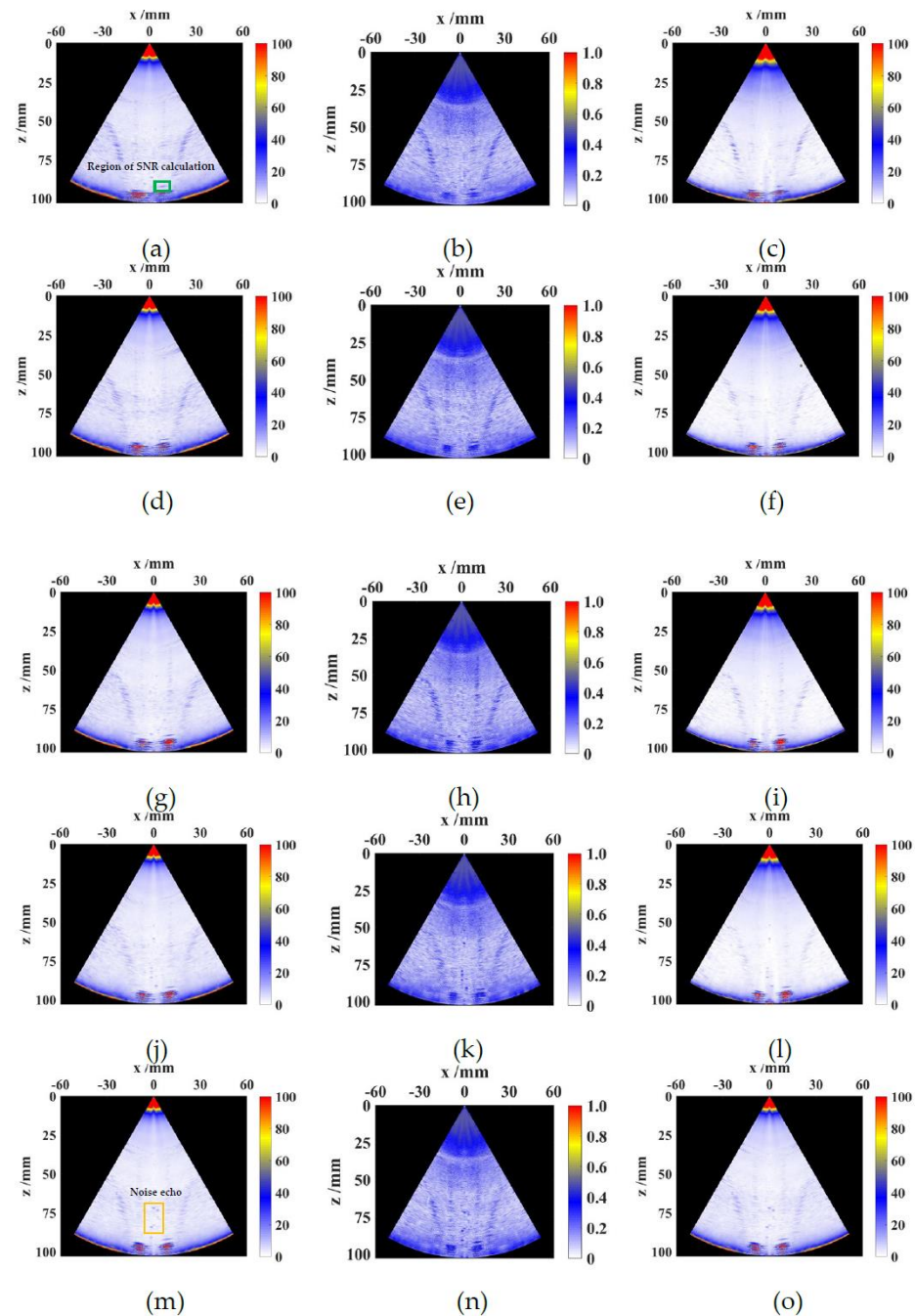


**Figure 8.** Imaging results of groove with depth 0.1 mm and buried depth 90 mm. (a) DAS, (b) VCF, and (c) DAS\_VCF with focus depth 30 mm; (d) DAS, (e) VCF, and (f) DAS\_VCF with focus depth 40 mm; (g) DAS, (h) VCF, and (i) DAS\_VCF with focus depth 50 mm; (j) DAS, (k) VCF, and (l) DAS\_VCF with focus depth 60 mm; (m) DAS, (n) VCF, and (o) DAS\_VCF with focus depth 70 mm.

#### 4.2. Image Quality with Different Focus Depth

The images of defects with different focus depths at the buried depth of 70 mm are selected to evaluate the image quality and verify the performance of the DAS\_VCF algorithms. The defects are selected with the green rectangle, and located in the center, as shown in Figures 7c and 8a. What is more, the area of interest region is  $2.8 \times 1.1$  mm while calculating the SNR, i.e., the area of the green rectangle. According to Equation (8), the SNR of defects with different focus depths is calculated. The SNR of cracks with DAS and DAS\_VCF algorithms are shown in Table 4.

**Table 4.** SNR of cracks with DAS and DAS\_VCF algorithms.

Algorithm	SNR (dB)				
	70 mm	60 mm	50 mm	40 mm	30 mm
DAS	12.99	13.69	11.90	11.77	11.24
DAS_VCF	23.76	25.36	23.16	22.58	19.03

Both SNR of cracks at the buried depth of 70 mm with DAS and DAS\_VCF algorithms increase with the focus depth increasing, as shown in Table 4. When the sound beam is focused at the depth of 30 mm, the focusing ability decreases with the propagation of the sound. Due to the target defect at the buried depth of 70 mm is far from the focusing range, the SNR of the traditional S-scan image is 11.24 dB and the lowest. Outside the focus region, the phase alignment of the echo signal from the target defect is low but still higher than the spurious signal. Hence, VCF weighting improves the SNR of the DAS image, according to the phase difference. When focusing depths at 60 mm and 70 mm, the focusing ability of the sound beam at the target defect is strong, and the SNR of the same algorithm is almost the same and reaches the maximum. Compared with DAS algorithms, in the case of the same focus depth with the same buried depth, the SNR of the crack is improved in images obtained by DAS\_VCF algorithms.

#### 4.3. Enhancement Effect of VCF Weighting with Different Focus Depths

The defect at the buried depth of 90 mm is selected to study the influence of focus depth with VCF weighting. The selected region is in a green rectangle, as shown in Figure 8. Both SNR of cracks at different focusing depths with DAS and DAS\_VCF algorithms are calculated and compared with the SNR of cracks of the buried depth at 70 mm. The SNR curve is drawn, as shown in Figure 9.

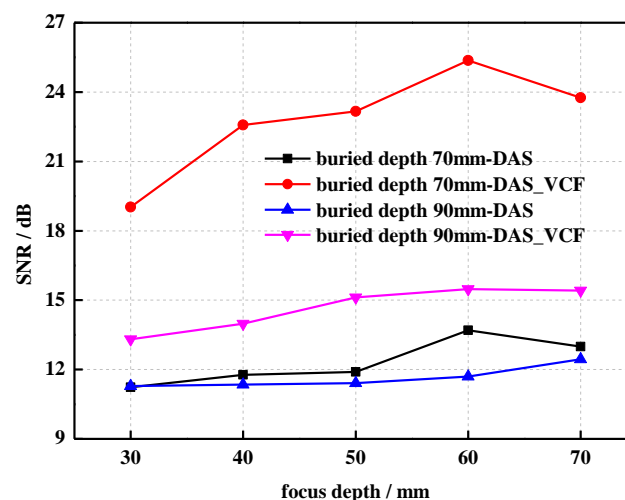


**Figure 9.** Comparison of SNR curve for defects with a buried depth of 70 mm and 90 mm.

As shown in Figure 9, the variation trend between the SNR value of crack at buried depth 90 mm and 70 mm is the same, and the SNR value increase with the focus depth

increasing. With the VCF weighting, the SNR value of DAS\_VCF is better than that of DAS. During the propagation processing, due to the beam's energy attenuation being serious at the large buried depth, makes the amplitude of defect echo received by the transducer is low and results in the SNR value of crack at the buried depth of 90 mm usually being lower than that of 70 mm in DAS images. Moreover, due to the focus region of the sound beam does not cover the defect by 90 mm, the phase consistency of defect echoes is dispersed. Hence, the VCF weighting effect of cracks at the buried depth of 90 mm is half that of the cracks at the buried depth of 70 mm.

Unlike the TFM and CPWC, sector scan imaging performs the test by the focusing sound beam. The focusing effect of the actual physical focus point is essentially different from that of the post-processed virtual physical focus of TFM and CPWC. In addition, active focusing is the signal acquisition strategy of sector scan imaging. Therefore, compared with the signal acquisition strategy of plane wave and full matrix capture, the coherence effect of defects is different in sector scan imaging. In addition, extracting instantaneous phases before and after receiving delayed processing will also lead to different phase coherence effects. It can be determined that the artificial groove of bolt shank cannot be detected, or even sidewall images of the bolt shank cannot be observed with TFM and CPWC under the same experimental conditions. Our research is only on sector scan imaging based on VCF weighting. The primary purpose is to improve the resolution and signal-to-noise ratio of traditional phased array sector scan imaging. Furthermore, this paper has analyzed the application of VCF factors in sector scan imaging. It hopes to enlighten the readers who study the imaging of such complex components, and more readers can recognize the application prospect of sector scan imaging based on VCF weighting.

## 5. Conclusions

This work has demonstrated the validity of crack detection with the depth of 0.1 mm at a deeply buried depth by combining vector coherence factor weighting with phased array ultrasonic S-scan imaging in the presence of crack detection of in-service bolt shanks. Moreover, the experimental result shows that the crack with 0.1 mm at the buried depth of 90 mm on the surface of the in-service bolt shank is detected efficiently by DAS algorithms. Furthermore, the image's background noise and the bolt shank's secondary echo are suppressed. Additionally, the SNR value of the crack in the DAS\_VCF images is improved after being weighted with the vector coherence factor compared with the DAS images. What is more, compared with DAS images, the SNR value of crack at the buried depth of 70 mm in DAS\_VCF images is improved by 11.67 dB with the focus depth at 60 mm.

**Author Contributions:** Conceptualization, J.H., M.C. and Y.C.; methodology, Q.K. and L.X.; software, Q.K. and Y.C.; validation, M.C., Q.K. and L.X.; formal analysis, C.L. and Y.C.; investigation, M.C. and L.X.; resources, J.H. and C.L.; data curation, Q.K. and Y.C.; writing—original manuscript preparation, J.H., M.C. and Q.K.; writing—review and editing, J.H., C.L. and Y.C. All authors have read and agreed to the published version of the manuscript.

**Funding:** This research was funded by the National Natural Science Foundation of China (Grant number 62161028, 51705232) and supported in part by the Natural Science Foundation of Jiangxi (Grant No. 20192BAB216026).

**Institutional Review Board Statement:** Not applicable.

**Informed Consent Statement:** Not applicable.

**Data Availability Statement:** Not applicable.

**Acknowledgments:** The authors would like to thank Key Laboratory of Non-destructive Testing Technology, Ministry of Education, Nanchang Hangkong University List for their help in the experimental setup.

**Conflicts of Interest:** The authors declare no conflict of interest.

## References

1. Suh, C.M.; Yuuki, R.; Kitagawa, H. Fatigue Microcracks in A Low Carbon Steel. *Fatigue Fract. Eng. Mater. Struct.* **2010**, *8*, 193–203. [[CrossRef](#)]
2. Noroozi, S.; Sewell, P.; Vinney, J. Investigation of Bolt Group Configurations on Load Distribution and Joint Failure. *Mech. Adv. Mater. Struct.* **2014**, *21*, 422–432. [[CrossRef](#)]
3. Ghang, L.; Hunebum, K.; Jongsung, W. Effectiveness of a Simplified Pullout Test Using a Post-Installable Break-Off Bolt. *Res. Nondestruct. Eval.* **2013**, *24*, 1–17.
4. Martin, V.D.; Craig, W.; Wilson, G.J. Non-destructive testing of materials subject to atmospheric stress corrosion cracking. *Insight* **2009**, *51*, 1–21.
5. Dubosc, P.; Chemin, P. Penetrant testing and year 2060. *Eur. Conf. Non-Destr. Test. Curran Assoc.* **2010**, *5*, 7–11.
6. Eisenmann, D.J.; Enyart, D.; Lo, C.; Brasche, L. In Review of progress in magnetic particle inspection. *AIP Conf. Proc.* **2014**, *1518*, 1505–1510.
7. Zhang, Y.F.; Gong, Y.Q.; Wang, Y.J.; Han, K. Analysis of non-destructive testing method for transverse crack of water wall of Supercritical Boiler. *IOP Conf. Ser. Earth Environ. Sci.* **2020**, *512*, 1–8. [[CrossRef](#)]
8. Beard, M.D.; Lowe, M.J.S. Non-destructive testing of rock bolts using guided ultrasonic waves. *Int. J. Rock Mech. Min. Sci.* **2003**, *40*, 527–536. [[CrossRef](#)]
9. Pollock, D.G.; Bender, D.A.; Soltis, L.A. Fasteners as damage indicators in timber structures. *Proc. Int. Wood Eng. Conf.* **1996**, *4*, 38–45.
10. Chen, J.Z.; He, R.Y.; Kang, X.W.; Yang, X.Y. Simulation and experiment for the inspection of stainless steel bolts in servicing using an ultrasonic phased array. *Nondestruct. Test. Eval.* **2015**, *30*, 373–386. [[CrossRef](#)]
11. Yang, S.; Yoon, B.; Kim, Y. Using phased array ultrasonic technique for the inspection of straddle mount-type low-pressure turbine disc. *NDT E Int.* **2009**, *42*, 128–132. [[CrossRef](#)]
12. Lu, J.; Chen, L.X. Phased array ultrasonic testing for in-service bolts of port machinery. *NDT* **2019**, *41*, 54–56.
13. Wang, W.Q.; Ma, G.B.; Wang, B.; Tang, J.B.; Zeng, C.M.; Xu, J.L. Study on Ultrasonic Inspection of Baffle Bolts in Nuclear Power Plants. *Nucl. Power Eng.* **2020**, *41*, 40–44.
14. Woo, C.S.; Hyun, L.J. Application of Ultrasonic Phased Array Techniques for Inspection of Stud Bolts in Nuclear Power Plants. *Solid State Phenom.* **2006**, *110*, 97–104.
15. Xue, L.J.; Liu, Q.Y.; Fang, Y.; Zuo, Y.T.; Yan, X.D. Imaging influence factors of phased array inspection for special equipment bolts in-service. *NDT* **2016**, *38*, 6–10.
16. Urbahs, A.; Carjova, K. Bolting Elements of Helicopter Fuselage and Tail Boom Joints Using Acoustic Emission Amplitude and Absolute Energy Criterion. *J. Aerosp. Eng.* **2019**, *32*, 04019005. [[CrossRef](#)]
17. Moles, M.; Ginzl, R. Phased Arrays for Detecting Cracking in Bolts. In Proceedings of the 6th International Conference on NDE for Structural Integrity for Nuclear and Pressurized Components, Budapest, Hungary, 8–10 October 2007.
18. Austeng, A.; Nilsen, C.-I.C.; Jensen, A.C.; Näsholm, S.P.; Holm, S. Coherent plane-wave compounding and minimum variance beamforming. In Proceedings of the 2011 IEEE International Ultrasonics Symposium (IUS), Orlando, FL, USA, 18–21 October 2011.
19. Kotowick, K.; Rohling, R.; Lampe, L. Adaptive compounding of synthetic aperture and compounded plane-wave imaging for fast ultrasonography. In Proceedings of the IEEE International Symposium on Biomedical Imaging, San Francisco, CA, USA, 7–11 April 2013; pp. 784–787.
20. Li, P.C.; Li, M.L. Adaptive Imaging Using the Generalized Coherence Factor. *IEEE Trans. Ultrason. Ferroelectr. Freq. Control.* **2003**, *50*, 128–141.
21. Synnevag, J.F.; Austeng, A.; Holm, S. Adaptive Beamforming Applied to Medical Ultrasound Imaging. *IEEE Trans. Ultrason. Ferroelectr. Freq. Control.* **2007**, *54*, 1606–1613. [[CrossRef](#)]
22. Zhang, J.; Drinkwater, B.W.; Wilcox, P.D. Comparison of ultrasonic array imaging algorithms for non-destructive evaluation. *IEEE Trans. Ultrason. Ferroelectr. Freq. Control.* **2013**, *60*, 1732–1745. [[CrossRef](#)]
23. Cruza, J.F.; Camacho, J.; Fritsch, C. Plane-wave phase-coherence imaging for NDE. *NDT E Int.* **2017**, *87*, 31–37. [[CrossRef](#)]
24. Hollman, K.W.; Rigby, K.W.; O'donnell, M. Coherence factor of speckle from a multi-row probe. *IEEE IUS* **1999**, *2*, 1257–1260.
25. Wang, Y.; Zheng, C.; Peng, H. Dynamic coherence factor based on the standard deviation for coherent plane-wave compounding. *Comput. Biol. Med.* **2019**, *108*, 249–262. [[CrossRef](#)]
26. Yang, C.; Jiao, Y.; Jiang, T.; Xu, Y.; Cui, Y. A United Sign Coherence Factor Beamformer for Coherent Plane-Wave Compounding with Improved Contrast. *Appl. Sci.* **2020**, *10*, 2250–2265. [[CrossRef](#)]
27. Chen, Y.; Kong, Q.R.; Lu, C.; Shi, W.Z.; Li, Q.F. Circular statistics vector weighting for ultrasound coherent plane wave compounding. *Chin. J. Sci. Instrum.* **2021**, *42*, 264–273.
28. Mao, Q.Q.; Chen, Y.; Zhang, B.Y.; Shi, W.Z.; Lu, C.; Li, Q.F. Enhancing effect of phase circular statistics vector for improvement imaging quality of ultrasonic total focusing method. *Acta Acust.* **2020**, *45*, 913–921.
29. Gauthier, B.; Painchaud-April, G.; Le Duff, A.; Belanger, P. Towards an Alternative to Time of Flight Diffraction Using Instantaneous Phase Coherence Imaging for Characterization of Crack-Like Defects. *Sensors* **2021**, *21*, 730. [[CrossRef](#)] [[PubMed](#)]